3-D flame temperature field reconstruction with multiobjective neural network

Xiong Wan (万 雄)[1,2], Yiqing Gao (高益庆)[2], and Yuanmei Wang (汪元美)[2]

[1] *Institute of Automation of Nanjing University of Aeronautics and Astronautics, Nanjing 210016*

[2] *Department of Test and Control Engineering, Nanchang Institute of Aeronautical Technology, Nanchang 330034*

Received August 21, 2002

A novel 3-D temperature field reconstruction method is proposed in this paper, which is based on multi-wavelength thermometry and Hopfield neural network computed tomography. A mathematical model of multi-wavelength thermometry is founded, and a neural network algorithm based on multiobjective optimization is developed. Through computer simulation and comparison with the algebraic reconstruction technique (ART) and the filter back-projection algorithm (FBP), the reconstruction result of the new method is discussed in detail. The study shows that the new method always gives the best reconstruction results. At last, temperature distribution of a section of four peaks candle flame is reconstructed with this novel method.

OCIS codes: 110.6960, 100.3010, 120.6780, 200.4260, 300.6170.

The multispectral (multiwavelength) radiation thermometry[1], which can be used to measure the true temperature and the spectral emissivity simultaneously, has been developed since recent years. There are three main mathematic models about multispectral radiation thermometry, namely: model based on measuring constant, model based on luminance temperature, and model based on reference temperature. Studies show that the model based on reference temperature has the least errors when it is used in measuring temperature and spectral emissivity[2]. Its principle is as follows:

If a temperature-measuring system uses n wavelengths, the channel voltage output V_i corresponding to the ith wavelength is proportional to the radiant intensity of the object $L(\lambda_i, T)$ according to Planck Law and can be expressed as

$$\begin{aligned} V_i &= A_{\lambda_i} \cdot L(\lambda_i, T) \\ &= A_{\lambda_i} \cdot \frac{C_1}{\pi} \cdot \varepsilon(\lambda_i, T) \cdot \left\{ \lambda_i^5 \left[\exp\left(\frac{C_2}{\lambda_i T} \right) - 1 \right] \right\}^{-1}, \end{aligned} \tag{1}$$

where $i = 1, 2, \cdots n$, and A_{λ_i} is a constant related to spectral responsibility of the photoelectric detector at wavelength λ_i and the property of the optical system. C_1 and C_2 are the first and second radiative constants, respectively. ε is the spectral emissivity of the object related to wavelength λ_i and temperature T.

If the temperature is lower than 3000 K, Eq. (1) can be approximately written as

$$V_i = A_{\lambda_i} \cdot \frac{C_1}{\pi} \cdot \varepsilon(\lambda_i, T) \cdot \lambda_i^{-5} \exp\left(-\frac{C_2}{\lambda_i T} \right). \tag{2}$$

The reference temperature is given by the blackbody furnace. Because the spectral emissivity is equal to 1, the channel output V_i' corresponding to the ith wavelength is

$$V_i' = A_{\lambda_i} \cdot \frac{C_1}{\pi} \cdot \lambda_i^{-5} \exp\left(-\frac{C_2}{\lambda_i T'} \right). \tag{3}$$

In terms of Eqs. (2) and (3), we can get

$$\ln\left(\frac{V_i}{V_i'} \right) - \frac{C_2}{\lambda_i T'} = -\frac{C_2}{\lambda_i T} + \ln \varepsilon(\lambda_i, T). \tag{4}$$

In multispectral radiation thermometry, there is a hypothesis

$$\ln \varepsilon(\lambda, T) = a + b\lambda. \tag{5}$$

If we define

$$\begin{cases} y_i = \ln\left(\frac{V_i}{V_i'} \right) - \frac{C_2}{\lambda_i T'}, \\ c = -\frac{C_2}{T}, \end{cases} \tag{6}$$

we have

$$y_i = a + b\lambda_i + c\lambda_i^{-1}, \quad (i = 1, 2, \cdots, n). \tag{7}$$

We only need to measure the ratio of the detector outputs under the true temperature T and the reference temperature T' to get the true temperature T and the spectral emissivity ε.

The method mentioned above is suitable for one point temperature measurement, and if we want to reconstruct a 3-D temperature field, we must combine the multispectral radiation thermometry with the computed tomography (CT) technique. A 3-D temperature field consists of many sections, therefore, if temperature distribution of each section is detected, the whole distribution of the 3-D temperature field will be known.

As shown in Fig. 1, the detector receives the signals which is the line integral of the radiant intensity $L(x, y)$ of all points in each section. Thus the output of the detector corresponding to certain wavelength can be expressed as

$$V_P(t, \theta) = A_{\lambda_i} \int L(x, y) \mathrm{d}s. \tag{8}$$

According to Eq. (2), Eq. (8) can be written as

$$V_P(t, \theta) = \int V_i(x, y) \mathrm{d}s. \tag{9}$$

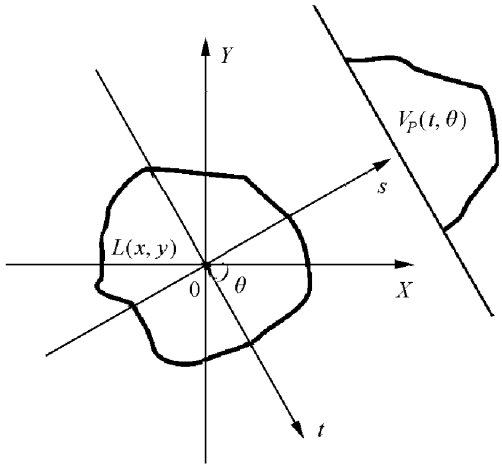

Fig. 1. The relationship of detector output and radiant intensity for every point.

So the output of the detectors is a Radon Transform of signal $V_i(x,y)$ of all points in each section. First, we get $V_i(x,y)$ according to the CT algorithm, then we can obtain temperature and spectral emissivity distribution of the 3-D field in terms of Eqs. (4) – (7).

Wang proposed a medical CT algorithm based on multiobjective neural network in recent years[3,4]. In our research, the algorithm is used and developed for the reconstruction of the $V_i(x,y)$ distribution.

If each section is divided into N ($N = q^2$) points, $\mathbf{V}$ is an N-dimensional vector needed to be reconstructed. According to series-expansion technique, we have a matrix formula to reconstruct $\mathbf{V}$

$$\mathbf{V_P} = \mathbf{WV} + \mathbf{E}, \tag{10}$$

where $\mathbf{E}$ is an M-dimensional vector of the errors which are due to the inaccuracy of the physical measurement, $\mathbf{V_P}$ is an M-dimensional detector output measurement vector and $\mathbf{W}$ is an $M \times N$ projection matrix.

The multiobjective reconstruction is estimating a vector $\mathbf{V}$ as the "solution" of Eq. (10) and the following equation is satisfied simultaneously

$$\min f(\mathbf{V}) = (f_1(\mathbf{V}), f_2(\mathbf{V}), f_3(\mathbf{V})), \tag{11}$$

where

$$\begin{cases} f_1(\mathbf{V}) = \gamma_1 \sum\limits_{l=1}^{N} (V_l \ln V_l), \\ f_2(\mathbf{V}) = \gamma_2 \sum\limits_{k=1}^{M} [\sum\limits_{l=1}^{N} W_{kl} V_l \\ \qquad \ln \left(\left(\ln \sum\limits_{l=1}^{N} W_{kl} V_l \right) / V_{Pk} \right)], \\ f_3(\mathbf{V}) = \frac{1}{2}\gamma_3 \left(\sum\limits_{l=1}^{N} V_l^2 \right), \end{cases} \tag{12}$$

where γ_1, γ_2, γ_3 are the normalized coefficients for various objective functions, respectively.

The first objective function $f_1(\mathbf{V})$ is the global smoothness of the image. The second objective function $f_2(\mathbf{V})$ is a measure of the cross entropy function between the original projection data and the reprojection data due to the reconstruction image. The third objective function $f_3(\mathbf{V})$ is the sum of the square norm of the image which is the measurement of the peakedness of the reconstructed image.

Because the weights of the three functions are different, the weighted method is used as

$$\min \phi(\mathbf{V}) = \sum_{j=1}^{3} w_j f_j(\mathbf{V}). \tag{13}$$

An analogue Hopfield neural network can be used to solve the multiobjective optimization problem in Eq. (13). Let the output variable v_l for neuron l be $0 < v_l < 1$ and let a continuous and monotonic increasing function of the internal state variable u_l of the neuron l be $v_l = q(u_l)$. Here

$$q(u_l) = [1 + \exp(-2u_l/\alpha)]^{-1}, \tag{14}$$

where α determines the steepness of function. Then the energy function can be expressed as

$$\begin{aligned} E(v) = \{ & w_1\gamma_1 \sum_{l=1}^{N} v_l \ln v_l \\ & + w_2\gamma_2 \sum_{k=1}^{M} \left[\sum_{l=1}^{N} W_{kl} v_l \ln \left(\sum_{l=1}^{N} W_{kl} v_l / V_{Pk} \right) \right] \\ & + \frac{1}{2} w_3\gamma_3 \sum_{l=1}^{N} v_l^2 \} \\ & + \frac{1}{2}\mu \left[(\mathbf{WV} - \mathbf{V_P})^T \mathbf{\Omega}^{-1} (\mathbf{WV} - \mathbf{V_P}) \right] \\ & + \sum_{l=1}^{N} \frac{1}{R_l} \int_0^{v_l} q^{-1}(v) \mathrm{d}v, \end{aligned} \tag{15}$$

where μ is a multiplier, and $\mathbf{\Omega} = \mathrm{diag}(\sigma_1^2, \cdots, \sigma_M^2)$ whose element represents the variance of the projection errors. Each neuron has an associated capacitance C_l and a resistance R_l ($R_l = C_l = 1$). The number of neurons in the network is N.

Thus, the following iteration process is obtained

$$\begin{aligned} & u_l(t + \Delta t) \\ & = u_l(t) + \Delta t \{ -u_l(t) - w_1\gamma_1 (1 + \ln v_l) \\ & \quad - w_2\gamma_2 \left[\sum_{k=1}^{M} W_{kl} \left(1 + \ln \sum_{l=1}^{N} W_{kl} v_l / V_{Pk} \right) \right] \\ & \quad - w_3\gamma_3 v_l \} \\ & \quad - \mu \sum_{k=1}^{M} W_{kl} \left(\sum_{l=1}^{N} W_{kl} v_l - V_{Pk} \right) / \sigma_k^2, \\ & \quad v_l(t) = q(u_l(t)), \quad l = 1, 2, \cdots, N. \end{aligned} \tag{16}$$

A stopping criterion is chosen

$$|v_l(t + \Delta t) - v_l(t)| < \varepsilon, \quad (\varepsilon \ll 1).$$

In order to estimate the reconstruction quality of the Hopfield neural network (HNN) algorithm, we select a

four-peaks-Gaussian function (Fig. 2), which can simulate a four-peaks temperature field and can be expressed as

$$\begin{aligned}&\text{FourGauss}(x,y)\\&=\sum_{l=1}^{4}a_i\exp\left[-\frac{4\ln 2}{0.2^2}(x-x_i)^2-\frac{4\ln 2}{0.2^2}(y-y_i)^2\right],\\&x_1=0.15,\ y_1=0.15;\ x_2=0.15,\ y_2=-0.15;\\&x_3=-0.15,\ y_3=0.15;\ x_4=-0.15,\ y_4=-0.15;\\&a_1=1,\ a_2=0.4,\ a_3=0.6,\ a_4=0.8.\end{aligned}\tag{17}$$

Then we compare HNN reconstruction results with those of the algebraic reconstruction technique (ART) and filter back-projection (FBP) algorithms[5−7]. We divide the reconstruction image into $26\times 26=676$ points. The projection data from 4 views and 51 rays in each view were generated for the simulation. The noisy projection data are generated as

$$\hat{V}_{Pk}=\left[1+N\left(\mu_0,\sigma^2\right)\right]V_{Pk},\quad(k=1,2,\cdots,204),$$

where V_{Pk} means the accurate projection data, N means a Gaussian probability distribution. We set $\mu_0=0$ and $\sigma^2=(0.03)^2$.

The reconstruction error is defined as

$$\alpha=\sum_l|V_l-V_l'|/(V_{\max}\times N),\tag{18}$$

where V_l is the four peaks Gaussian function, V_l' is the reconstruction data.

The results of the three algorithms are shown in Table 1 and the plot of HNN reconstruction is shown in Fig. 3, which show significantly less error when the HNN algorithm is compared to the other two algorithms under the same noisy projections.

The experiment device for 3-D temperature field reconstruction is shown in Fig. 4. It consists of a rotation platform, four Sony DP-75 color digital cameras and four peaks candle flames.

The basic wavelengths of the color digital cameras are 700 nm (red), 546.1 nm (green), and 436.8 nm (blue), respectively. The reference temperature of the blackbody furnace is $T'=1200$ K. We can reconstruct the 3-D flame temperature field with multispectral radiation thermometry and HNN CT algolrithm.

One of the experiment results is shown in Fig. 5, which denotes the temperature distribution of the flame section that is 17 cm higher than the platform.

Computer simulation and experiment results show that the projection data and the fine reconstruction results can be easily obtained by the method proposed in this

Table 1. Reconstruction Error (%)

Algorithm	HNN	ART	FBP
α	1.05	1.56	12.65

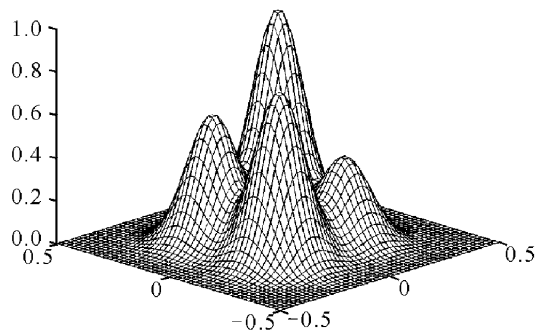

Fig. 2. Four peaks Gaussian function.

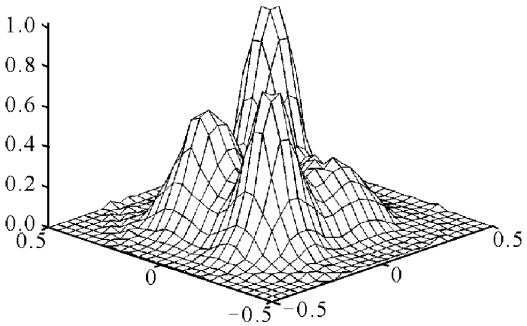

Fig. 3. Reconstruction result of HNN algorithm.

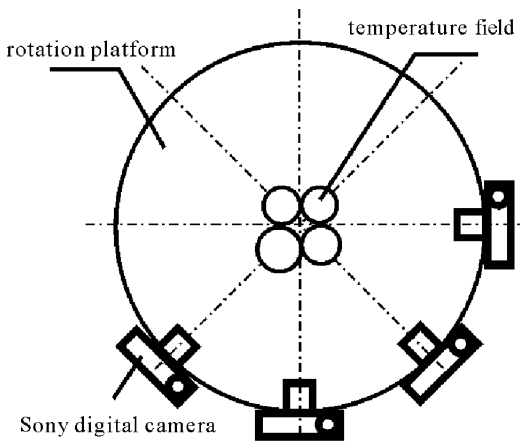

Fig. 4. 3-D temperature field reconstruction experiment.

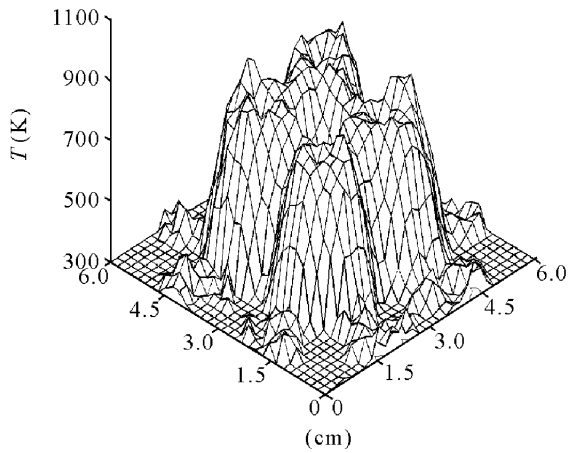

Fig. 5. Certain flame section temperature distribution.

paper, predicting a fine prospect of this method in 3-D temperature field reconstruction.

This project was supported by China Aeronautical Basic Science Foundation under Grant No. 00I56004 and by Foundation of Jiangxi Test Technology and Control Engineering Center under Grant No. KG200104002. X. Wan's e-mail address is wanxiong1@163.net.

References

1. J. M. Dai and Z. X. Zhu, J. Infrared Millim. Waves **14,** 461 (1995).
2. X. G. Sun, The theory and experiment of multispectral (multiwavelength) radiation thermometry, in Doctorial Dissertation of Harbin Institute of Technology (1998) p. 12.
3. Y. M. Wang and W. X. Lu, Signal Processing **26,** 17 (1992).
4. Y. Wang and F. M. Wahl, IEEE. Proc: Vis. Image Signal Process **144,** 233 (1997).
5. Y. Q. Gao, Chin. J. Lasers B **5,** 150 (1996).
6. D. Verhoeven, Appl. Opt. **20,** 3736 (1993).
7. N. Ohyama, S. Ohki, S. Inoue, J. Tsujiuchi, and T. Honda, JOSA A **4,** 318 (1987).